Materials & Design 265 (2026) 115903

Contents lists available at ScienceDirect

Materials & Design

journal homepage: www.elsevier.com/locate/matdes

Resilience throughout Hierarchy: What makes pili nuts (*Canarium ovatum*) so tough?

Shajia Afrin Ali [a,*], Max David Mylo [b,c,d], Jonathan Perrin [e], Timm Weitkamp [e], Thomas Speck [b,c], Claudia Fleck [a,*]

[a] Chair of Materials Science & Engineering/Fachgebiet Werkstofftechnik, Institute of Materials Science and Technology, Faculty III - Process Sciences, Technische Universität Berlin, Str. Des 17. Juni 135 - Sekr. EB 13, 10623 Berlin, Germany
[b] Cluster of Excellence LivMatS @ FIT—Freiburg Center for Interactive Materials and Bioinspired Technologies, University of Freiburg, Georges-Köhler-Allee 105, 79110 Freiburg, Germany
[c] Plant Biomechanics Group @ Botanic Garden Freiburg, University of Freiburg, Schänzlestr. 1, 79104 Freiburg, Germany
[d] Department of Microsystems Engineering—IMTEK, University of Freiburg, Georges-Köhler-Allee 103, 79110 Freiburg, Germany
[e] Synchrotron SOLEIL, L'Orme Des Merisiers, Départementale 128, 91190 Saint-Aubin, France

ARTICLE INFO

Keywords:
Nutshells
Hierarchical structure
Mechanical behavior
Digital image correlation
Finite element simulation
Bioinspiration
Biomimetics

ABSTRACT

Cracking the endocarp of pili nuts is no easy task – it requires pre-notching or the expertise of skilled workers to open the shell. This difficulty arises from its exceptional strength and toughness, which are due to its hierarchical structure and form. We combine various imaging techniques, mechanical testing, and computational modelling to elucidate the relationship between micro- and macrostructure and mechanical properties. Compression tests with digital image correlation on whole and half nuts, along with finite element simulations, show how shell geometry influences the strain distribution and, thus, crack initiation and propagation. The three-sided bipyramidal shape provides high stability of the endocarp under compression, due to optimized load distribution. Simulations predict regions of maximum principal stresses. In brittle materials, cracks are likely to initiate here as the tensile strength is exceeded first. This hypothesis is corroborated by our lab tests on half-nuts. Toughening mechanisms operate at the macro-scale, deflecting cracks along weak interfaces in the sandwich structure. Thus, the hierarchical design – combining a strong though brittle base material with weaker interfaces deflecting cracks, and a geometry that evenly distributes loads – offers inspiration for lightweight, robust composite containers made from materials otherwise inherently prone to sudden, catastrophic fracture.

1. Introduction

Through evolutionary processes, natural materials with remarkable combinations of strength, toughness, and light weight have emerged. But how can engineers leverage the structural principles observed in Nature to create better and more sustainable designs? Translating natural strategies into engineering innovations, that is, transferring structure-property-relationships, is a possible and promising strategy [1]. Among the most impressive materials in Nature are nut- and seed shells – many of them light yet incredibly strong and tough. Not only do they protect the seed from everyday environmental influences, but they also provide remarkable resistance to stabbing and impact, making them ideal blueprints for designing puncture-resistant and energy-absorbing materials [2–4].

A striking example is the endocarp – colloquially referred to as the (nut-)shell – of the pili fruit (*Canarium ovatum*), a tropical drupe native to the Asia-Pacific region. With an exceptionally hard-to-crack endocarp, the nuts are usually sold pre-notched along with a special tool designed to assist in opening (**Fig. 1a**). There is no evidence of animals able to break the shell to access the seed. The forces required to fracture whole nuts under compression have been reported to range from 1.60 to 3.15 kN, depending on load orientation and moisture content [5]. Compared to their average wall thickness, these shells are stronger than those of peanuts, hazelnuts, walnuts, and almonds [3], with only the coconut endocarp, the shells of some other palm species, macadamia seed coats, and the mesocarp of Brazil nuts outperforming them in strength [3,4,6].

To gain insight into the structural origins of the exceptional strength

* Corresponding authors.
E-mail addresses: shajia.a.ali@tu-berlin.de (S.A. Ali), claudia.fleck@tu-berlin.de (C. Fleck).

https://doi.org/10.1016/j.matdes.2026.115903
Received 9 September 2025; Received in revised form 28 February 2026; Accepted 21 March 2026
Available online 23 March 2026

of pili nuts, we previously analyzed the hierarchical organization of the pili fruit. We identified eight morphologically distinct levels (Table 1), spanning from the organ level of the entire fruit (H0) down to the molecular scale (H7) [7]. Macroscopically (H2), the endocarp has an oval to lanceolate shape with a nearly triangular cross-section and rounded corners (Fig. 1**a**) [7–9]. It usually contains one large fertile locule with the seed inside and two empty sterile locules (Fig. 1**b**) [7,8]. On the next level (H3), the endocarp is built of seven concentric tissue layers (Fig. 1**b**) [7]. For clarity, the layers extending from the inner epidermis to the crystal layer are collectively referred to as "inner sclerenchymatous tissue", whereas the remaining layers are summarized under the term "outer sclerenchymatous tissue". This dense, multilayered sandwich structure contains fibers in various directions, thus resembling a fiber-reinforced composite material. While sharing several features with other hard nut- and seed shells, the multilayered architecture of the pili nut endocarp is much more compact. Unlike the vascular network seen in macadamia seed shells [3] or larger defects observed in the Brazil nut mesocarp [4], the pili endocarp contains only a single central vascular bundle (Fig. 1**b**) in one corner of the triangular shell, housed loosely in a relatively large cavity in the most dominant, outer sclereid layer [7]. Furthermore, the local fiber orientations differ from those of the other shells, and we found an additional "crystal layer" containing semicircular structures rich in silicon and resembling a string of pearls [7].

Our previous mechanical tests on millimeter-sized specimens extracted from the non-locular side of the endocarp (highlighted in blue in Fig. 1**b**) revealed values for the Young's modulus between 2322 MPa and 3905 MPa for tension and compression alike, while the compressive strength is three to four times higher than the tensile strength (**Table S1**) [7]. At the microstructural level (H4), the cellular material fails in a brittle manner, suggesting it is optimized for high strength, with cracks propagating through sclerenchymatous cells without evidence of fiber pull-out [7]. This material forms the basis of a sandwich structure (H3), which features a weak interface between the crystal layer and the inner sclereid layer. This weak interface induces shear failure during compression [7].

While compression testing provides a straightforward method for measuring the force required to crack nutshells, understanding the internal stress and strain distribution and identifying critical failure points remain challenging. Existing knowledge provides analytical solutions for stress distributions in thin-walled shells with boundary conditions corresponding to specific geometries. These solutions apply to spherical shells with radius (R) to thickness (t) ratios of $R/t \simeq 30$ compressed between rigid plates [10]. Some researchers have addressed the contact problem between spherical shells with different thickness ratios and a flat surface, analyzing scenarios with $R/t \simeq 50$ and $\simeq 10$ [11]. The shape of the pili nutshell is not only non-spherical but also characterized by $R/t \simeq 4$ (based on the geometric mean diameter and mean shell thickness), thus deviating considerably from the studied geometries and the conditions for known analytical solutions. Numerical approaches such as the finite element method (FEM) provide an alternative approach for calculating stresses, deformations, and strains, and even allow the prediction of fracture strength in materials [12]. Geometric data derived from 3D imaging provides a highly detailed basis for FEM modelling, enabling the incorporation of intricate structural details in complex geometries. Validation of strain fields in such studies can be achieved through mechanical experiments coupled with digital image correlation (DIC) [13,14].

We previously reported on the compression behavior of macadamia seed coats and Brazil nut mesocarps, simulated using FEM with linear elastic material properties. We used simplified ellipsoid geometries and compared these with models based on micro-computed tomography (μCT) data, which also included internal voids. Laboratory compression tests with DIC measurements of the strain fields were used to validate the computational results. We identified circumferential tension as the key factor in nut failure, while internal voids were found to redistribute stress and absorb energy, hindering crack growth [15]. Another study used data from a 3D laser scanner to perform a dynamic FE simulation of the walnut cracking process with an ordinary nutcracker, applying orthotropic linear-elastic, ideally brittle material properties. The study highlighted the need to improve the design of this nutcracker to minimize plastic deformation [16]. Following a similar approach, researchers simulated the static compression of hazelnuts between two rigid plates [17]. The results indicated that an equivalent stress of

Table 1
Hierarchical levels (HL) and the entities within. For a more detailed description, see [7].

Level	HL	entities
organ	H0	fruit
organ	H1	pericarp, seed
organ	H2	exo-, meso-, endocarp, testa, kernel
tissue	H3	all layers in the endocarp (Fig. 1b), vascular bundle
cells	H4	sclereids, sclerenchymatous fibers, tracheids
sub-cellular structures	H5	cell walls, cell lumens
sub-cellular structures	H6	cell wall layers, pits
molecular level	H7	chemical elements

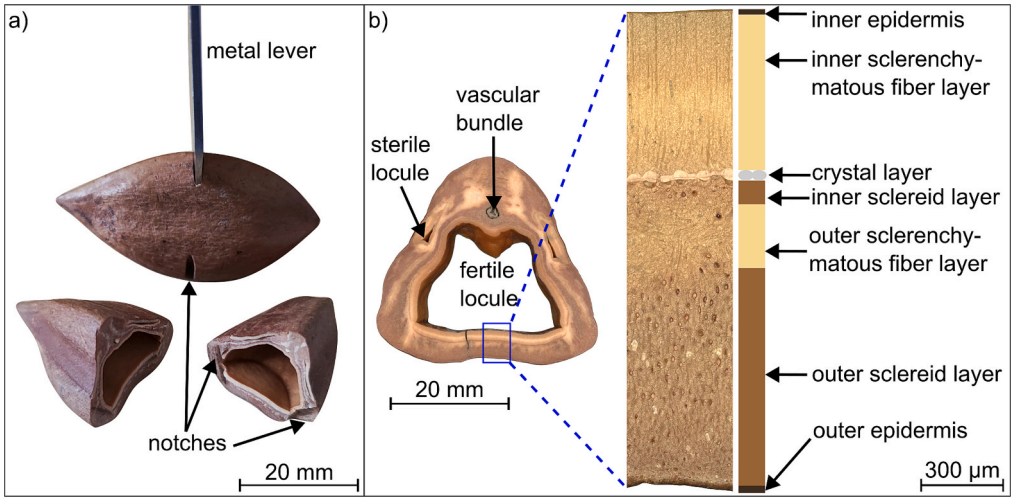

Fig. 1. The pili nut endocarp: a) Commercial cracking method using a flat metal lever (H2); b) layered tissue structure (H3) in cross-section, visualized using digital optical microscopy [7]. We summarize all layers from the inner epidermis to the crystal layer as "inner sclerenchymatous tissue" and refer to the remaining layers as "outer sclerenchymatous tissue".

approximately 10 MPa was required to crack the nut. Further, a pecan nut was modelled to simulate a high-speed impact scenario. This simulation showed that stresses around 7 MPa and an impact force of about 1000 kN were required to initiate a crack in the pecan shell [18].

In summary, the relationship between the intricate structure and the exceptional mechanical failure resistance of the pili nutshell remains largely unresolved. To address this knowledge gap, we investigated the properties of pili nuts across different hierarchical levels. Here, we identify critical regions for failure based on stress and strain distributions, evaluated during compression loading of whole and half nuts and derived from both experimental and computational testing. We correlate compression properties and structural failure at the level of the whole shell with our previous results on morphometric, morphological, and anatomical characteristics, as well as on mechanical properties in tension and compression at the material level [7].

2. Results

2.1. Force-displacement curves of whole and half nutshells under compression

Force-displacement curves from compression tests performed in the laboratory ("*in vitro*" tests) and from FE simulations ("*in silico*" tests) with four different loading scenarios reveal pronounced differences in the compressive behavior between whole and half nuts on the one hand, and between loading directions on the other hand (Fig. 2**a–d**). The maximum forces and their corresponding displacements, including mean, median, and standard deviation, from the laboratory experiments are summarized in **Table S2**.

In the *in vitro* transverse loading cases (Fig. 2**a and c**), the force steadily increases to a peak for both whole and half nuts. This is followed by a sudden, sharp force drop, after which the force exhibits a decreasing serrated pattern. The mean maximum force of half nuts is approximately

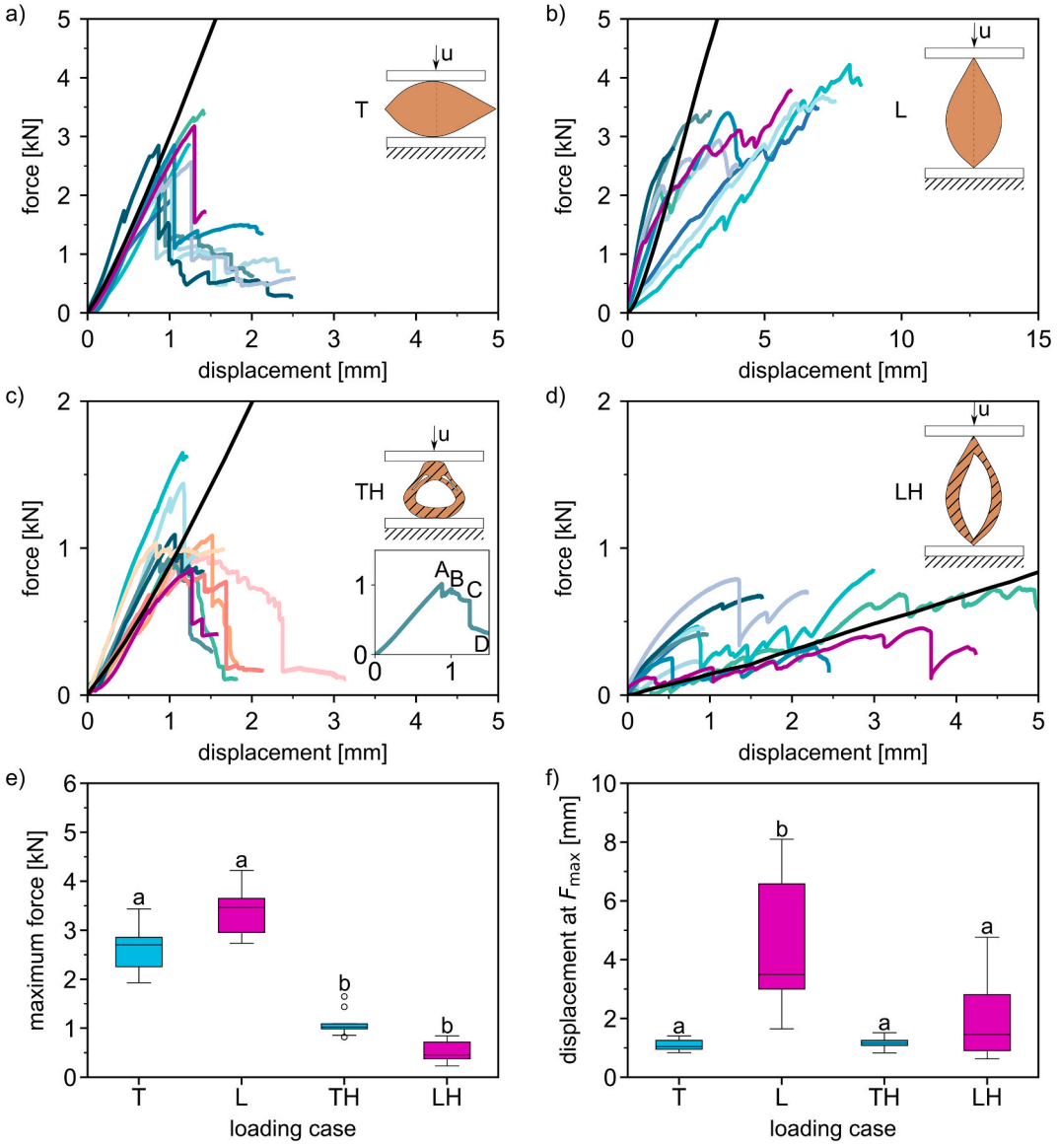

Fig. 2. Force-displacement curves from 10 experiments for each of the four nut compression scenarios: **a, b)** Whole nuts loaded in **a)** transverse (T), **b)** longitudinal (L) direction; **c, d)** half nuts loaded in **c)** transverse (TH), **d)** longitudinal direction (LH). The magenta curves highlight the experiments in which the displacement was evaluated with 3D DIC. Orange (and magenta) colors in panel c indicate half nuts on the apical side. The other curves represent the remaining experimental results. The black curve represents the simulation results. Boxplots illustrate the distribution of **e)** the maximum forces (F_{max}), and **f)** the displacements at F_{max} for each loading case. Significant differences between scenarios are denoted by letters a and b. Identical letters indicate groups with no significant difference. (For interpretation of the references to colour in this figure legend, the reader is referred to the web version of this article.)

60% of the value measured for whole nuts (**Table S2**). Furthermore, the first force drop is less pronounced for the half nuts and is followed by fluctuations displaying an overall decreasing trend. The half nuts from the basal side (light blue/turquoise curves) exhibit slightly stiffer behavior than those from the apical side (orange and magenta curves). Notably, the mean displacement at the maximum force is similar for whole and half nuts in this loading direction (**Table S2**).

Videos of the tests on the half nuts allow us to correlate the force-displacement course with information on crack formation and growth patterns. The inset in Fig. 2**c** shows a typical force–displacement curve of a half nut; the corresponding test is shown in **Video S1**. The initial load drop (marked "A" in Fig. 2**c** and **Video S1**) coincides with the first visible formation of a rather large crack in the non-locular region (pink arrow in **Video S1**). This crack traverses the outer sclerenchymatous tissue and the interface between the inner and outer sclerenchymatous tissues. Shortly thereafter, the force increases slightly until an additional crack forms within the inner sclerenchymatous tissue (yellow arrow). Subsequently, another crack initiates at the lower corner of the right sterile locule (green arrow). During this stage, the force continues to increase, although with a slightly decreasing slope. At timepoint B, a pronounced crack forms within the inner sclerenchymatous tissue (purple arrow) beneath the vascular bundle, accompanied by a slight drop in force. This is followed by a serrated plateau in the curve, during which the crack at the corner of the sterile locule (green arrow) propagates, with occasional deflections, toward the inner sclerenchymatous tissue. It is redirected at the interface, while the outer wall of the sterile locule undergoes buckling. The inner sclerenchymatous tissue in the non-locular region progressively separates from the neighboring tissue (yellow arrow), accompanied by a drop in force. This force is then sustained up to timepoint C, when an additional crack initiates at the outer lower left corner (blue arrow), resulting in another force drop. Finally, the force decreases continuously until the inner sclerenchymatous tissue (yellow arrow) becomes completely detached at timepoint D.

In contrast to the transverse loading scenarios, the nuts loaded in the longitudinal direction (Fig. 2**b and d**) show force fluctuations already during the first loading stages before the force reaches an absolute maximum. Because in this loading scenario the load was applied through the pointed ends of the nuts, most of them exhibited intermittent, slight slipping during compression, which occasionally resulted in a minor tilt of the nut. At the same time, pronounced crumbling of the tip region was observed directly at the contact area from the early stages of loading, progressively increasing the contact area at the load introduction site and leading to recurring force drops. After the global force has increased continuously to a maximum, it drops abruptly (force drop not shown for clarity). Two characteristic groups of curve progression are observed: one group with a lower slope, and another one with a steeper increase in force.

For the half nuts (Fig. 2**d**), the fluctuations of the force during the overall rising part of the curve are more pronounced, and the average maximum forces are 85% lower than for the whole nuts (**Table S2**). The corresponding mean displacement is 66% lower (**Table S2**). In general, whole nuts exhibit stiffer behavior when compressed in the longitudinal as compared to the transverse direction, while the opposite is true for half nuts.

The simulation results (black curves in Fig. 2**a–d**) agree well with the elastic deformation behavior observed in the *in vitro* experiments for the transverse loading cases (Fig. 2**a and c**). As expected, – since the geometry model for the transverse half nuts represents the apical side – the simulated curve is in better agreement with the corresponding experimental results (Fig. 2**c**, black versus magenta & orange curves).

Ignoring the force fluctuations in the experimental results for whole nuts tested in the longitudinal direction (Fig. 2**b**), the simulated curve provides a reasonable overall approximation, particularly for the stiffer nuts. In contrast, the simulated curve of the half nut loaded in the same direction (Fig. 2**d**) predicts a less stiff response compared to the initial, presumably linear-elastic section of the experimental curves.

The boxplots in Fig. 2**e and f** highlight the variability in the maximum forces and the corresponding displacements. The highest median maximum force (Fig. 2**e**) is observed for whole nuts loaded longitudinally, with similar interquartile ranges (IQRs) for both loading directions. For half nuts, the median is higher in the transverse direction, and the scatter is lower, as indicated by a smaller IQR than in the longitudinal direction. Three outliers are identified in the transverse group: two with markedly higher values and one slightly below the typical range. Overall, the IQR for half nuts is smaller than that of whole nuts. A Kruskal-Wallis test ($\chi^2 = 34.57$, $p < 0.05$) confirms that the differences in maximum force across loading conditions are statistically significant. According to Dunn's post-hoc test, these differences are significant between whole and half nuts within the same loading direction, while no significant differences are found between the two loading directions within the whole or half nut group.

Regarding the displacements at maximum force (Fig. 2**f**), the highest median and IQR are observed for whole nuts loaded longitudinally. This also applies to half nuts, though with lower values than for whole nuts in the same direction. In contrast, the medians and IQRs for transverse loading are similar for both whole and half nuts. A Kruskal-Wallis test ($\chi^2 = 19.28$, $p < 0.05$), followed by Dunn's post-hoc analysis, reveals that only the longitudinal loading of whole nuts differs significantly from all other loading cases. Although the median displacement for half nuts loaded longitudinally is slightly higher than for those loaded transversely, the difference is not statistically significant due to the large data scatter.

2.2. Strain distribution in whole and half nutshells under compression

Fig. 3 compares the DIC-derived and FE-calculated principal strain fields (major and minor strains) for all loading scenarios at a compressive displacement of 4% relative to the original nut height or length. Transverse compression of the whole nut (Fig. 3**a and b**) results in a pronounced compressive deformation in the upper contact area (arrows 1) and the concave region of the nut (arrows 2), while the convex region at the rounded corner of the cross-section experiences tensile strains (arrows 3). The results for the half nuts (Fig. 3**c and d)** also reveal compressive strains in the contact area (arrows a). Additionally, we observe compressive strains around the sterile locules (arrows b). The inner top and bottom regions are under tensile strain (arrows c), while the bottom inner corners experience compressive strain (arrows d). In both transverse loading cases, the experimental and simulation results are in very good agreement and even provide similar strain values.

In the longitudinal loading case, the upper and lower tips of the shells, i.e., both contact areas, experience high compressive strains for both whole (arrows 1 in Fig. 3**e and f**) and half nuts (arrows a in Fig. 3**g and h**). Notably, in contrast to the DIC measurements, the simulation of the whole shell predicts a concentrated region of high tensile strains just below the tip at the upper contact area (arrow 2 in Fig. 3**e**). In the concave region of the nutshell (arrows 3 in Fig. 3**e and f**), the simulation predicts tensile strains that are in good agreement with the DIC measurements. For half nuts, the simulation shows a pronounced compressive strain in the sectioned plane at the front (arrows b). Tensile strains are seen towards the back of the shell (arrows c in Fig. 3**g and h**). While the trend is similar in the experiment, the measured strain magnitude is smaller.

2.3. Failure patterns of whole and half nutshells under compression

Under transverse compression, whole nuts show two different fracture patterns. In some nuts, a part of the nutshell broke off completely (Fig. 4**a**), with the fracture surfaces oriented parallel to the loading direction. The fracture surface usually traversed a sterile locule (arrow 1 in Fig. 4**a**). Other nuts only broke in the middle, parallel to the loading direction (not shown). In most cases, the seed could not be extracted after failure. SEM images of the fracture surfaces (Fig. 4**b**) reveal a high

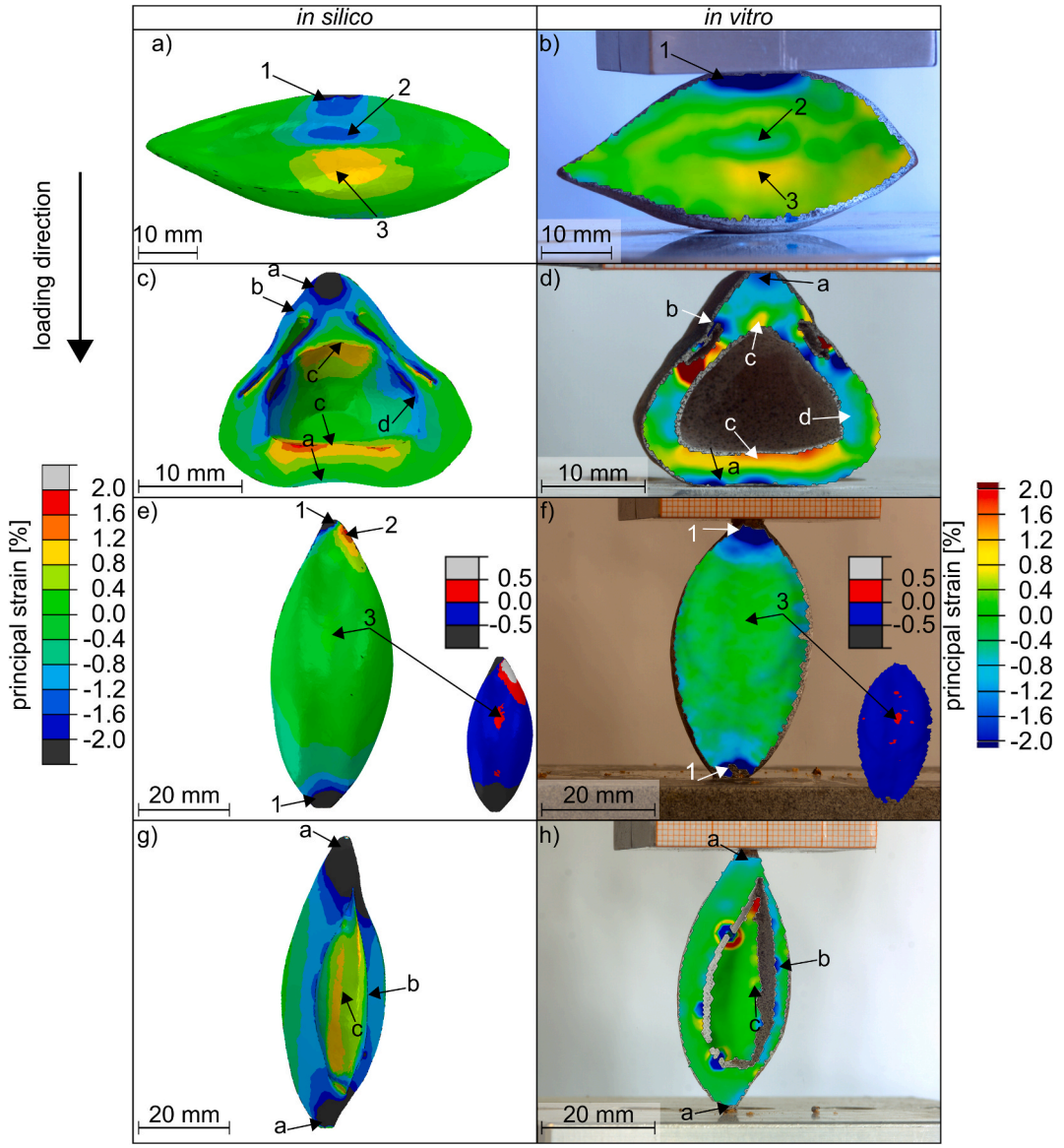

Fig. 3. Principal strain fields for different loading scenarios of the pili nutshells at 4% compressive displacement relative to the original nut length: Left images **(a, c, e, g)** show the simulation results (*in silico*), right images **(b, d, f, h)** depict the 3D DIC results (*in vitro*) of **a, b)** whole nut, transverse loading; **c, d)** half nut, transverse loading; **e, f)** whole nut, longitudinal loading; **g, h)** half nut, longitudinal loading. The colors represent the magnitude of the major and minor strains, depending on which strain values are higher in absolute value.

number of sclerenchymatous fibers aligned parallel to the fracture surface.

For the half nuts (Fig. 4**c**), the fracture pattern is described in detail in Section 2.1 (**Video S1**). The main cracks appear in the non-locular (arrow 1) and the sterile-locule region (arrows 2 and 3), and at the top of the fertile locule (arrow 4). At a smaller scale, the SEM micrograph of the upper sterile locule corner (marked with a pink square) shows further that cracks are deflected along the sclerenchymatous fibers (arrows in Fig. 4**d**).

Typically, under longitudinal loading, the whole nuts fractured into two (Fig. 4**e**) or three (not shown) fully separated pieces, allowing complete extraction of the seed. The cracks or fractures were oriented parallel to the loading direction and consistently passed through the concave sides of the nuts, regardless of whether sterile locules were present (arrow 1 in Fig. 4**e**) or absent (arrow 2 in Fig. 4**e**). SEM observation of the fracture surfaces revealed that the sclerenchymatous fibers were aligned parallel to the fracture plane (Fig. 4**f**). In contrast to complete fracture, some nuts only crumbled at their pointed ends (not shown).

Half nuts under longitudinal loading typically exhibited failures at the tips (Fig. 4**g**). These fractures ranged from minor crumbling (not shown) to complete fracture of one tip after bending (arrow 1 in Fig. 4**g**), resulting in an uneven fracture surface (Fig. 4**h**) with sclerenchymatous fibers torn in various directions.

3. Discussion

Pili nuts exhibit remarkable strength and fracture resistance. To elucidate the reasons for these properties, we combined (micro-)structural investigations with mechanical testing and FEM. Our results highlight the influence of the hierarchical and highly anisotropic structure on the mechanical performance of the pili nut endocarp.

From a biological viewpoint, the question arises why such a remarkable strength is necessary. Pili nut dispersal relies on a variety of frugivores. In particular, hornbills are believed to effectively disperse seeds over long distances after eating the ripe fruits [8], and other

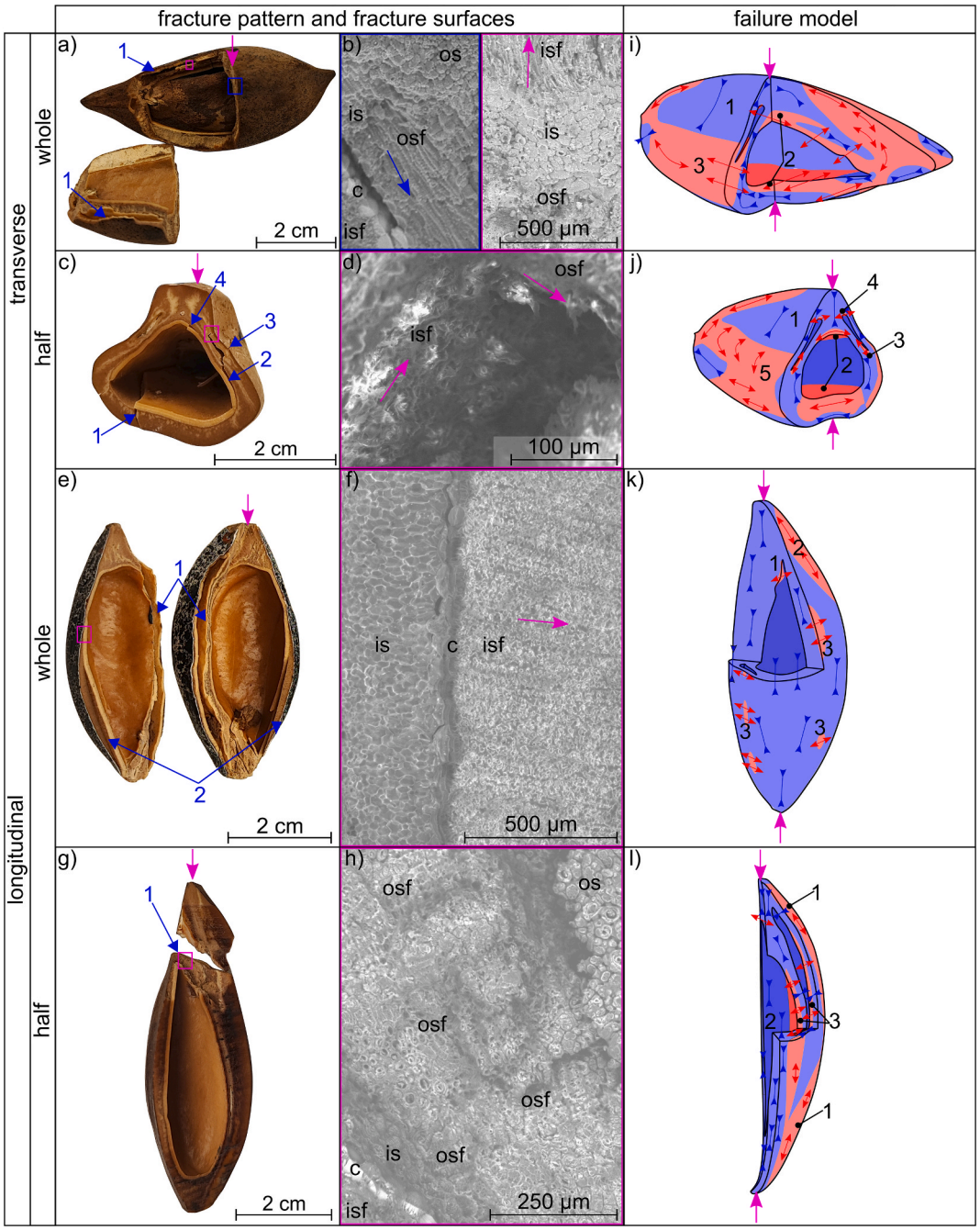

Fig. 4. Transverse or longitudinally compression-loaded whole and half nutshells: **a, c, e, g)** Digital images of fracture patterns. Pink arrows indicate the loading direction. **b, d, f, h)** SEM micrographs of typical fracture surfaces, marked in the digital images by pink or blue squares. Arrows highlight fiber orientations; "os" = outer sclereids, "of" = outer sclerenchymatous fibers, "is" = inner sclereids, "c" = crystal, "if" = inner sclereid fibers. **i – l)** Absolute maximum principal stress distributions obtained from FEM simulations. Red indicates tensile stresses and blue compressive stresses, depending on which principal stress has the greater absolute magnitude. (For interpretation of the references to colour in this figure legend, the reader is referred to the web version of this article.)

animals, such as monkeys, wild pigs, wild deer, and rodents, are also known to consume the pulp of ripe fruit [8]. Notably, all these animals expel the nuts, and no animal is known to be able to crack the shells [8]. It is therefore very likely that, from an evolutionary perspective, the high strength prevents the seeds from being cracked and digested, thus securing their dispersal.

3.1. *Mechanical properties in comparison with other nutshells*

Compared to other nut- and seed shells, both stiffness and fracture strength of the pili nut endocarp are among the highest values measured across a broad group of such shell materials (Table 2). Its Young's modulus [7] is comparable to that of the Brazil nut mesocarp [19–22]. Only macadamia shells surpass these stiffness values by a factor of 2, while all other listed species exhibit notably lower moduli. Regarding strength, pili and macadamia have similar values, whereas Brazil nuts are harder to crack. This is, to a great extent, due to wall thickness, which is higher in Brazil nuts than in pili and macadamia shells. When the fracture forces of these nutshells are normalized by the mean wall thicknesses, pili nuts are still outperformed by the other two species. Peanut, pecan, walnut, hazelnut, and almond shells are all considerably weaker [3,4].

Table 2
Fracture forces (F_{frac}) and Young's moduli (E) of various nutshells under quasi-static loading in the transverse direction with information on their moisture content (q) and their mean shell wall thickness (t_{mean}). The pili nut data is from this and our previous [7] work. Other data is based on [3] unless stated otherwise. The three highest values of mechanical parameters are marked in bold.

species	q [wt %]	t_{mean} [mm]	F_{frac} [N]	F_{frac}/t_{mean} [N mm^{-1}]	E [MPa]
pili nut	5.7 ± 0.7	4.5 [7]	**2637 ± 458**	**586 ± 102**	**2322 – 3905** [7]
peanut	2.0 ± 0.5	1.2	76 ± 20	63 ± 17	0.3–6.7 [39]
pecan	5.5 ± 0.9	1.2	323 ± 114	269 ± 95	34.3–122.2 [18]
walnut	5.1 ± 0.3	1.6	378 ± 165	236 ± 103	42.7–71.8 [16]
hazelnut	5.5 ± 0.1	1.5	431 ± 127	288 ± 85	44.0–86.1 [17]
almond	4.9 ± 0.1	3.2	895 ± 181	280 ± 57	no data
macadamia nut	10.1 ± 0.7	2.3	**2364 ± 645**	**1016 ± 105**	**4185 – 5200** [20,21]
Brazil nut	9.7 ± 0.3 [4]	6.3 [4]	**10079 ± 1460** [4]	**1605 ± 232** [4]	**2300–4000** [22]

In contrast to the other shells, the wall thickness of the pili nut varies substantially: it is highest at the solid apex (~5.7 mm), and reaches a minimum of ~2.8 mm in the region of the sterile locules, when they are ignored (that is, they are interpreted as full material). If the empty space is considered, the values are even smaller: ~1.4 mm at the inner walls of the sterile locules and ~0.9 mm at their outer walls. Normalizing the fracture forces by these lower values yields even higher strength values (by a factor of 1.6 and 3 to 5, respectively). Surprisingly, however, first cracks often do not start in these thinnest regions (compare **Video S1**). These seemingly counterintuitive observations will be discussed in detail in Section 3.2.1.

3.2. *Deformation and failure mechanisms of whole and half nutshells under compression*

In tension and compression tests, we previously observed predominantly brittle failure in millimeter-sized specimens extracted from the endocarp of pili nuts [7]. Thus, at the microstructural level (H4), the material seems optimized for high strength. Only in compression did we see a sign of a toughening mechanism: delamination along the crystal layer. This suggests that the sandwich structure (H3) may contribute to toughness through crack deflection and energy dissipation at coarser structural levels, such as whole and half nutshells (level H2). While DIC measurements provide information only on major and minor surface strains, FEM simulations also determine internal stress distributions. Therefore, based on the surface information, DIC is a very valuable method for validating FEM simulations of biological structures and their underlying assumptions. Our *in silico* simulation experiments show a very good overall agreement with the *in vitro* experiments. Naturally, due to the chosen boundary conditions and material property assumptions, local deviations remain. Using the maximum normal stress criterion, our simulations elucidate how absolute maximum principal stresses and their directions govern crack initiation and failure in the shell (Fig. 4**i–l,** Fig. 5**a–e**).

3.2.1. *Transverse loading case*

When considering the directions of the absolute maximum principal stresses, two main behaviors emerge: i) Compression loading (Fig. 4**i, 1**) leads to tensile stresses orthogonal to the loading direction both inside the shell (Fig. 4**i, 2**) and on the outside near the sterile locules (Fig. 4**i, 3**). (ii) Additionally, the change in stress orientation across neighboring regions, together with the local transition between compressive- and tensile-dominated states, promotes shear at the boundaries, such as between the concave and convex shell regions (Fig. 4**i, 1 and 3**).

When examining critical sites prone to failure (Fig. 5**a**), compressive stresses exceed the ultimate compressive strength at the contact points. This results in local flattening of the shell where the load is applied (arrow 1 in Fig. 3**b**). Regions where tensile stresses become critical are located at the bottom (Fig. 5**a, 1**) and top (Fig. 5**a, 2**) of the fertile locule. Earlier simulation increments (**Fig. S1a**) show that region 1 reaches critical stress levels first (Fig. 5**a**), suggesting internal crack initiation in the non-locular region – parallel to the loading direction, according to the direction of the tensile stress (Fig. 4**i, 2**). This internal initiation cannot be confirmed experimentally for whole nuts with our methods – such a proof would rely on 3D imaging where it is, however, questionable that the onset of cracking could even be tracked, because of the fast crack growth. Nevertheless, we provide indirect evidence from the half-nut experiment, which supports the prediction that the initial crack will occur in the non-locular region (pink and yellow arrows, **Video S1**).

Tensile stresses also become critical at and around the sterile locules (Fig. 5**a, 3**). In addition to the locally reduced wall thickness, the sharp geometric transitions at the locule boundaries act as stress concentrators (notch-like features). We may safely assume that this geometry facilitates crack initiation and subsequent growth. Furthermore, the outer shell region around the sterile locules may promote a crack initiation and propagation parallel to the loading direction (Fig. 4**i, 3**), due to the critical tensile stresses (Fig. 5**a, 3**) that are directed perpendicular to the loading direction. Such a crack is indeed observed in the fracture patterns (Fig. 4**a**), and the behavior is consistent with the fibrous microstructure of the shell. The long axis of the sclerenchymatous fibers is orthogonal to the tensile stresses, and we indeed observe cell separation along their interfaces (Fig. 4**b**, blue box).

The predominant fracture surface after shell detachment remains parallel to the loading direction (arrow 1 in Fig. 4**a**). However, the crack propagates in a direction perpendicular to the initially described fracture, leading to the detachment of a sizable fragment. This behavior is driven by shear stresses between region 1 and region 3 (Fig. 4**i**), which favor this failure mode. Once initiated, these cracks propagate preferentially along interfaces between sclerenchymatous fibers (Fig. 4**b**, pink box).

Other authors performed transverse compression tests on whole nuts and reported lower fracture forces (1.6 kN) than our results (2.6 kN) [5], and the seed remained unexposed. It is surprising that our strength results are nevertheless higher. This is most likely due to differences in the moisture content of the nuts during testing (6% in our work vs. 11–25% in [5]).

Turning to the transverse compression experiments on half nuts, we observed a stiffer response of the basal half compared with the apical half (Fig. 2**c**). The basal half tended to tilt from the beginning, resulting in a larger contact area.

The stress distribution for the half nut in Fig. 4**j** — which closely resembles that of the whole nut — shows that compressive loading (1) induces tensile stresses perpendicular to the loading direction at the top and bottom of the fertile locule (2). Tensile stresses are also present along the lower ends of the sterile locules (3) and near their upper end (4). In addition, a tensile region (5) occurs in the outer convex shell adjacent to the sterile locule, where the tensile stresses are oriented parallel to the loading direction.

From the principal stress distribution (Fig. 5**b**), we see that critical tensile stresses are present at the bottom of the fertile locule (Fig. 5**b, 1**), at the sterile locules (Fig. 5**b, 2**), and at the top of the fertile locule (Fig. 5**b, 3**), while critical compressive stresses occur at the upper contact region and lower corners of the sterile locules (Fig. 5**b, 4**). In our experiments, the contact region primarily showed local flattening of the shell (**Video S1**). Regarding critical tensile stresses, earlier simulation increments (**Fig. S1b**) show that regions 1 and 2 reach critical tensile stress levels before the other locations. Thus, the first crack is most likely

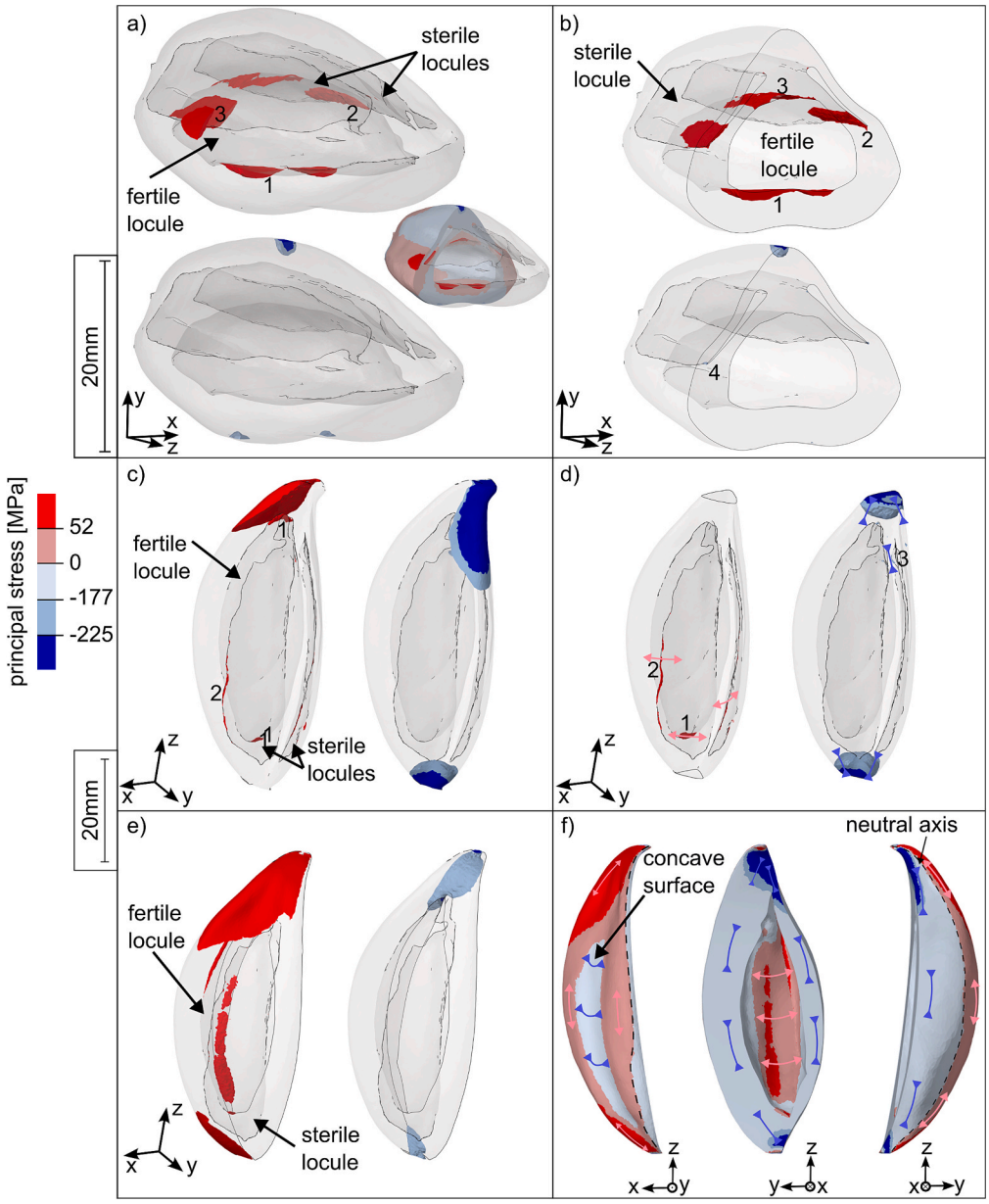

Fig. 5. Isoplots of absolute maximum principal stress distributions and the corresponding deformations obtained from FEM simulations, scaled for localized critical regions where the principal stresses exceed the tensile and compressive strength limits: **a, b)** Transverse loading up to 5% macroscopic compressive strain: **a)** whole nut, **b)** half nut; **c** – **e)** Longitudinal loading up to 8% macroscopic compressive strain: **c)** whole nut, **d)** whole nut with flat ends, **e)** half nut. Tensile (positive) stresses are shown in red, and compressive (negative) stresses are marked in blue. For each region, the stress component with the larger absolute value is displayed. **f)** Detailed stress distribution of the half nutshell, highlighting the resulting bending situation with the neutral axis and the tensile and compressive stress regions. (For interpretation of the references to colour in this figure legend, the reader is referred to the web version of this article.)

to be initiated in the non-locular region, as is evident in **Video S1**. The initiation surface (interface vs. outer sclerenchymatous tissue) cannot be determined without high-speed imaging. However, the second crack in the same region (yellow arrow in **Video S1**) shows a larger opening on the inner side, which is consistent with inside-to-outside propagation within the inner sclerenchymatous tissue. In region 2 (Fig. 5**b**), the tensile-critical stresses combined with the notch-like geometry of the sterile locules suggest crack initiation in this area. Consistently, a crack is observed there in the experiment (green arrow, **Video S1**, Fig. 4**c**, arrow 2). Likewise, in the tensile-critical area at the top of the fertile locule (Fig. 5**b, 3**), a crack is visible (purple arrow, **Video S1**). The cracks observed around the sterile locule (pink box and arrow 3 in Fig. 4**c**) are linked to the tensile regions in Fig. 4**j** (regions 3–5), which become critical after the initial crack occurred at the sterile locule (green arrow, **Video S1**).

So far, the critical regions have been identified based on the simulation results. However, the layered (sandwich-like) architecture of the shell provides additional insights, particularly in this loading case. In our previous work, we identified a weak interface between the crystal layer and the inner sclereid layer [7]. Together with the simulation results, this suggests that the first crack (pink arrow in **Video S1**) most likely originated at this weak interface within the non-locular shell region. This is also supported by another specimen (**Fig. S1c**), in which we observed that the crack is widest near the interface and gradually becomes narrower toward the outer sclerenchymatous tissue. A study by [23] corroborates our observations and assumptions, revealing that in heterogeneous material systems, interfaces between tissues with contrasting elastic moduli are favored sites for fracture initiation, whereas

in homogeneous structures, pre-existing defects are the primary origins of failure. The results of our previous nanoindentation tests show that the crystals and sclereids in our samples differ in elastic modulus by a factor of three [7], providing an additional mechanical explanation for the observed crack initiation at this interface.

As discussed, crack initiation in the shells is determined by the interplay between stress hotspots, influenced by the loading conditions, geometry, and local material strength. Despite the inherently brittle nature of the shell material, the local microstructure plays an important role. As shown in **Video S1**, cracks are deviated from a straight path through the ~4 mm thick shell at the inner interface along the crystal layer, thereby increasing the fracture energy and leading to a more benign failure behavior. This deviation lengthens the crack path by about 100% to 8 mm (pink arrow in **Video S1**), thus doubling energy dissipation. Additionally, the crack trajectory is locally deflected by sclerenchymatous fibers, further increasing energy dissipation (see e.g. the crack path at the lower corner of the sterile locule in **Video S1** (green arrow) and the SEM micrograph of the fracture surface near the upper corner (Fig. 4**d**)).

The events during crack formation and growth lead to serrations in the force–displacement curves. Notably, for both whole and half nuts, the force increases after crack initiation ("pre-failure event", e.g., after timepoint A in Fig. 2**c**). This may be due to interlocking or stress redistribution; however, further investigation is needed to fully explain this phenomenon. Such "pre-failure events" have also been observed in several other plant tissues [24–26]. They are an important contribution to a benign fracture behaviour and markedly increase the critical strain and the energy necessary for cracking.

3.2.2. *Longitudinal loading case*

For the longitudinal loading case, we observed a higher scatter in the fracture forces of the whole nuts (Fig. 2**b**). Two main factors contribute to this variability. First, the behavior is highly dependent on the natural variability of the nut ends. Blunter ends distribute the load over a larger contact area. This results in a more stable loading position and a stiffer reaction. Conversely, pointier ends have a smaller contact area, which can cause the nut to slip or tilt under load. Second, force drops indicate premature damage or crumbling of the pointed ends under high local compressive stresses, occurring before the nut reaches its global critical failure load.

Despite differences in boundary conditions and load introduction, our results align well with the literature. In particular, despite employing a compression jig with conical notches supporting the pointed ends, [5] reported comparable fracture forces and fracture patterns. Thus, slight sliding of the nuts appears to influence stiffness but not fracture force or failure progression.

Tensile stresses orthogonal to the loading direction that appear at the sharp inner corner of the shell due to its stress-raising effect likely led to the fracture pattern observed in a typical nut (Fig. 4**e, k, 1**). At this sharp inner notch, analysis of the principal stresses (Fig. 5**c, 1**) shows critical tensile stress concentrations (Fig. 5**c, 1**), suggesting crack initiation. Additional critical stresses are observed at the sterile locules (Fig. 5**c, 2**), indicating further potential crack initiation sites. Cracks are then assumed to propagate outward toward the concave areas (Fig. 4**k, 3**), parallel to the loading direction, near the sterile locules. Depending on how uniformly the force is introduced and where weak spots coincide with high tensile stresses, the nut will thus split into two or three pieces (Fig. 4**k, 3**). At the microstructural level, fracture occurs parallel to the long fiber axis of the cells in the inner sclerenchymatous fiber layer (Fig. 4**f**).

The simulation predicts bending near the tip regions (Fig. 4**k, 2**). However, this deformation mode has not been observed experimentally. The real nuts experience local crumbling at the pointed ends. This modifies the boundary conditions and effectively increases the contact area, in turn resulting in a more even strain and, consequently, a more even stress distribution. This can be roughly approximated by loading a nut model with the tips removed, creating artificially blunter ends (Fig. 5**d**) and thus eliminating the strong bending effect. In this model, the tensile strength is exceeded at the bottom of the fertile locule (Fig. 5**d, 1**), where the wall is thinner, due to the proximity to the sterile locules. Additionally, in a small, isolated region on the upper side of the sterile locules (Fig. 5**d, 3**), compressive stresses exceed the ultimate strength, potentially leading to failure.

Even though the half nutshells also have a notch near the tip, bending is their dominant failure mode (Fig. 4**l**). Due to the lack of symmetry, the outer portion of the shell experiences tension (Fig. 4**l, 1**), while the inner portion undergoes compression (Fig. 4**l, 2**). This bending mode is visible in the DIC results **(**Fig. 3**h)** and is predicted by the simulation. It is particularly evident in the tensile-compressive stress distribution shown in Fig. 5**f** and **Video S2**. Both tensile and compressive stresses exceed the corresponding ultimate strengths near the tips (Fig. 5**e**). This either leads to tip failure due to bending, resulting in an uneven fracture surface (Fig. 4**h and g**), or to crumbling of the tips. Furthermore, the additional tensile-critical region at the fertile locule (Fig. 5**e**) may promote cracking parallel to the loading direction (Fig. 5**f**, middle), a behavior observed only once in our experiments.

The uneven bending-induced fracture surface reveals different fiber orientations, which explains its roughness. Some fiber strands are oriented parallel to the loading direction, while others are aligned orthogonal to it. In the region surrounding the sterile locules, tensile stresses perpendicular to the loading direction (Fig. 4**l, 3**) are accompanied by orthogonal compressive zones (Fig. 4**l, 2**), which likely enhance shearing effects and help explain the observed angled fracture surface.

Note that the simulations represent the elastic state, and that simulations including crack formation and growth might reveal a different picture. Under these circumstances, it is remarkable how well the simulations reproduce the fracture states, possibly due to the inherent brittleness of the material. The force–displacement curve from the simulation of the half nut (Fig. 2**d**) follows the overall trend of the experimental data after the initial linear-elastic phase. As expected, the numerical model does not capture the serrated character of the experimental curves, since it does not account for slipping or crumbling at the tips. In the experiments (Fig. 2**d**), the less stiff curves are primarily associated with pronounced slipping, which reduces effective load transfer and thus lowers the global slope of the force–displacement response. Conversely, the steeper curves correspond to configurations in which the nuts remain stable during compression, enabling a more efficient load path. The observed force drops in the experimental curves indicate distinct local failure events, where the tips noticeably crumble or small fragments detach. Following such a drop, the force may rise again if the nut remains in a stable position and the contact area with the loading plates increases.

When comparing the force–displacement curve of the simulation with the experiments (Fig. 2**d**), a similar trend is observed: in the FEM, the low slope of the force–displacement curve is primarily due to tip bending, whereas in the experiments, even though a stiffer behavior is observed in the beginning, shell crumbling in combination with slipping locally reduces the load-bearing capacity, thus reducing the global slope of the force–displacement curves.

3.3. *Mechanical advantages of triangular and pyramidal shapes*

The DIC strain field of the half nut cross-section showed the characteristic deformation behavior of a triangular shape **(**Fig. 3**c and d**). Triangles are well-known for their sturdiness compared to other shapes due to their ability to distribute applied forces evenly across their edges [27]. When compressed from the top at one corner, the sides are compressed while the base is stretched, resulting in a stiff structure. Despite the curved geometry and the presence of locular cavities associated with sterile locules, the principal strain distribution of the half nut (Fig. 3c and d) shows a qualitatively similar pattern (Fig. 3**c and d**). In 3D, the

nut resembles a bipyramidal shape, which contributes to its bending stiffness when compressed in the longitudinal direction (Fig. 3**f**) and leads to an even load distribution. The advantages of a triangular (or tetrahedral) shape compared to other geometries can be demonstrated through both its internal kinematic determinacy and strain energy.

As outlined in **Appendix A.1**, the concept of kinematic determinacy can be further illustrated by comparing pin-jointed frameworks composed of rigid members with different levels of internal kinematic determinacy (Fig. 6**a**) [28]. According to **Eq. A1,** only the triangular configuration is internally kinematically determinate. Square and circular frameworks contain internal mechanisms and can change shape without member elongation (Fig. 6**a**).

Extending the planar reasoning to three dimensions (**Eq. A2**) likewise shows that the tetrahedron is kinematically determinate, whereas cubes or sphere-like frameworks are kinematically indeterminate.

In contrast to the previous, purely kinematic analysis, we now allow elastic deformations of the members, including both axial stretching and bending (Fig. 6**b**). Here, we consider vertical loading of each structure with the first-order theory for small deformations [29]: a triangular framework with a member length a and a height h is loaded at its apex C, a square framework with a member length h is loaded between opposing corners (D-C), and a circular framework with the diameter h is loaded at a single node (Fig. 6**b**). **Eq. A20** and **Eq. A24** show that the strain energies of square (axial + bending) and circular (bending-dominated, rotationally stiff nodes) frameworks both exceed that of the triangular framework (axial only) for slender members; a detailed derivation of these strain energies is provided in **Appendix A.2**.

3.4. Model assumptions and limitations

Overall, the results of our simulations agree well with our experimental findings: the force–displacement curves (particularly for the transverse loading case), and the strain distributions match those observed in the compression tests without and with DIC, respectively.

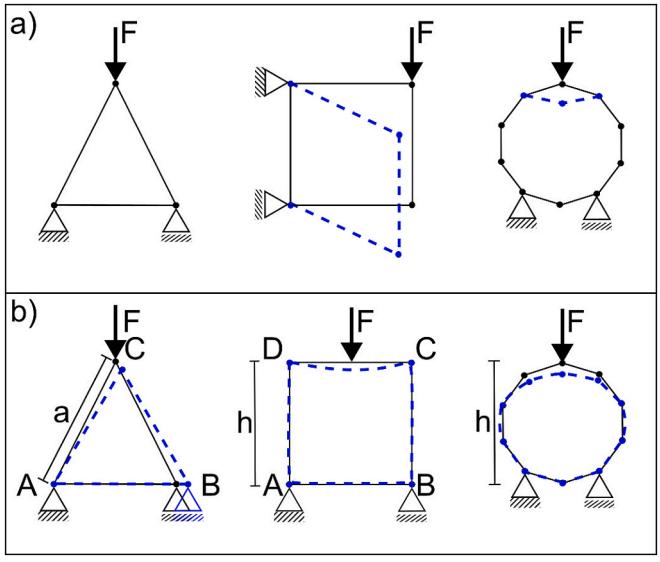

Fig. 6. Comparison of the kinematic response and deformation behavior of idealized 2D geometric structures under two mechanical assumptions: **a)** Illustration of the kinematic determinacy of a structure, showing how internal constraints govern the range of possible deformations. In this case, the members cannot deform. The black lines denote the members and the dots the joints of the structure. The blue lines indicate the shape after loading. **b)** Schematic of the deformation of each shape if deformation of the members is allowed, to illustrate the differences in strain energy. (For interpretation of the references to colour in this figure legend, the reader is referred to the web version of this article.)

Thus, despite employing isotropic linear-elastic material properties, the simulation model effectively captures the geometry-driven deformation patterns of the pili nutshell. Even the "hot spots" of stress and strain very well predict the failure origins seen in the experiments, despite the model neglecting the layered microstructure and time-dependent deformation. Nevertheless, in order to localize these "hot spots" more precisely, a model representing the heterogeneous shell structure is required.

Given the currently available material data, it is not possible to create such a model, as layer-resolved material properties are required. In principle, such data could be estimated from our previously published nanoindentation results using analytical relationships [7]. However, such estimates are based on several simplifying assumptions (e.g., isotropy and uniform porosity distribution, without accounting for pore morphology) [7]. Therefore, further experimental investigations – such as layer-specific tensile and compression tests, and micro-indentation – are required to determine reliable mechanical properties for each individual layer. We therefore used an effective homogenized modulus based on mechanical testing of millimeter-sized specimens, and simplified estimates for layered composites [7].

Establishing layer-specific, anisotropic material properties that accurately reflect cell geometry, porosity, and fiber orientation remains part of our ongoing work.

4. Conclusion

The endocarp of pili nuts is remarkably difficult to crack, combining exceptional strength, toughness, and puncture resistance with a complex geometry. This unique combination makes the entire nut a compelling model for bioinspired structural design. By correlating morphology, microstructure, and mechanical behavior across multiple length scales, we identified the following key findings and showed that the shell exhibits a scale-dependent mechanical behavior:

- H2 – bipyramidal shape and triangular cross-section: The bipyramidal shape provides stability and resistance to bending of the nut in the longitudinal direction, making it difficult to load the nut without tilting, and fostering loading in the transverse direction. In the transverse direction, the triangular cross-section ensures an even load distribution. Tensile stresses are the primary cause of fracture, with the ultimate tensile strength of the shell being markedly lower than its ultimate compressive strength [7].
- H3 – sandwich structure with weak interfaces: The layered arrangement with weak interfaces promotes crack deflection and energy dissipation, enhancing toughness and failure resistance. In particular, the interface between the crystal layer and inner sclereid layers plays a key role.
- H4 – cells: At the cellular level, the material behaves in a brittle manner [7]. However, under compressive loading of whole and half nuts, some fibers deflect cracks, thereby contributing to toughening. Under natural conditions, the higher humidity in the tropical environment of the Philippines (mean annual temperature 27 °C, mean annual humidity 80%) likely reduces brittleness [8].

To what extent does the mechanical performance support functional-morphological or evolutionary hypotheses about the protective role of the shell? Suppose the high strength provides protection against predators or against damage when lying on the ground. In that case, the slightly lower forces required to crack the nuts in the transverse direction are counterintuitive, as this is the expected loading direction. However, despite the slightly lower strength, it was nearly impossible to extract the seed in a single loading event in this direction.

Our previously suggested hypothesis for the structure–function strategy in the pili nut endocarp [7] – a high-strength, though brittle "base" material arranged in layers with weak interfaces and formed into a shape that evenly distributes loads – has been confirmed by our

compression tests on whole shells. Thus, we provide direct evidence for the functional role of the bipyramidal shape and the triangular cross-section. Our findings highlight the potential of an adapted design, inspired by the pili nut endocarp, for failure-resistant containers made from inherently brittle, high-strength materials.

5. Materials and methods

5.1. Material

Pili nuts were sourced from Allen, Northern Samar, and the Manama Food Forest, Kidapawan City, Cotabato, Philippines. The moisture content of the nuts was measured gravimetrically on 40 fractured pieces extracted from each of the 40 pili nutshells used for compression testing. The pieces were weighed using a standard analytical balance (0.002 g accuracy, 0.001 g resolution, Mettler Toledo PM1200, Mettler-Toledo GmbH, Giessen, Germany) before and after heat treatment at 60 °C for 24 h. The mean moisture content of the tested nut pieces was 5.7 ± 0.7%.

5.2. Compression tests on whole and half nutshells and digital image correlation

Compression tests were performed on nine pili nuts at the University of Freiburg, Germany, using a Hegewald & Peschke Inspekt retrofit (Hegewald & Peschke GmbH, Nossen, Germany), based on an Instron 4466 machine equipped with a 10 kN load cell (relative force resolution between 0.01% and 0.1% and a relative force deviation between −0.16% and 0.10%). All tests were conducted with a crosshead speed of 1 mm min^{-1} at room temperature. Seven whole nuts were tested, four in the transverse and three in the longitudinal loading direction; one half nut was tested in the transverse direction, and another half nut in the longitudinal direction. To stabilize the specimens upright for the longitudinal loading cases, preloads of ~120 N and ~23 N were applied to the whole and half nuts, respectively. Once an 80% reduction from the preceding force value was detected, the tests were terminated.

For 3D DIC analysis, a stereo camera setup was used consisting of two identical PL-D685CU cameras (Edmund Optics Inc., Barrington, NJ, USA; sensor pixel size 4.8 μm) equipped with macro planar lenses (T × 2 100 mm-1 ZF, Carl Zeiss AG, Oberkochen, Germany) oriented at a stereo angle of about 25° and at a distance of approximately 83 cm from the nuts. Compression tests were recorded using Capture OEM software (v.2.3.7.9, Pixeink, Rochester, NY, USA) at 2 fps, with an exposure time of 400 to 500 ms. Calibration of the system using intrinsic and extrinsic camera parameters was performed on the basis of 13 stereo images of a calibration panel (GOM CQ2-30 × 24) in different orientations. Each nut was prepared before the experiments with a white acrylic paint base coat, followed by a black stochastic pattern to enhance brightness and contrast for the DIC analysis. The deformations were evaluated and visualized using the GOM Aramis Professional software (GOM GmbH, Braunschweig, Germany) with a facet size of 19 x 19 pixels and a facet distance of 16 pixels.

Additional compression tests were performed to achieve a total of 10 nuts per load case, with a crosshead speed of 1 mm min^{-1} at room temperature, thereby strengthening the statistical analysis. These additional tests were conducted at Technische Universität Berlin, Germany, using a different universal testing machine (UPM—Inspect Retrofit 1475, 100 kN load cell with 0.5% accuracy, Zwick, refurbished by Hegewald & Peschke Meß- und Prüftechnik GmbH, Nossen, Germany).

5.3. Statistics

To assess data normality, Shapiro-Wilk tests [30] were conducted on the maximum force, and their corresponding displacement values from compression tests of both whole and half nuts, with comparisons made between loading directions (Fig. 2**e and f**). Furthermore, Levene's test [31] was applied to assess the homogeneity of variances.

Due to non-normal distribution, the Kruskal-Wallis test [32] with Dunn's post-hoc comparisons [33] was performed for maximum forces and their corresponding displacements. The significance level was set at 5% ($p < 0.05$) for all statistical analyses.

5.4. Microscopy and tomography

One polished specimen has been imaged with a digital microscope (Keyence VHX-7000, Keyence Deutschland GmbH, Neu-Isenburg, Germany) to show the layered sandwich structure (Fig. 1**b**). Fracture surfaces from compression tests on whole and half nuts (Fig. 4**b,d,f and h**) were examined by SEM (FEI Quanta 400 FEG, Thermo Fisher Scientific, FEI Deutschland GmbH, Frankfurt a. M., Germany) at 20 kV and 50 Pa in backscattered electron mode.

For FEM modeling, a μCT scan of a medium-sized nut was acquired at a voxel size of 26.6 μm on a *Phoenix* Nanotom scanner (180 kV, 20 W; GE Measurement & Control, Billerica, USA).

5.5. Finite element simulation

FE models were generated based on μCT data of the medium-sized pili nutshell. The seed was excluded from the model because its contribution to compressive strength was assumed to be negligible, as with macadamia nutshells [34]. Following μCT data segmentation with the open-source software 3D Slicer [35], the nutshell geometry was exported as a Surface Transformation Language (STL) file and converted into a model using Autodesk Fusion 360 (Autodesk GmbH, Munich, Germany). This model was meshed with linear volumetric tetrahedral elements (C3D4) in HyperMesh (v. 2022.3, Altair Engineering Inc., Troy, Michigan, USA). The meshing process generated 843,887 elements for the whole nutshell, 422,330 elements for the half nut sectioned in the transverse plane (from the apical side), and 664,130 elements for the half nutshell sectioned in the longitudinal plane. To incorporate the experimentally observed collapse of the pointed ends (**Section 2.1**) and the associated increase in contact area in the longitudinal configuration, an additional whole-nut geometry with artificially blunted ends was created (830,656 elements).

ABAQUS software (v. 2022, Dassault Systèmes, SIMULIA, Waltham, Massachusetts, USA) was used to perform FEM simulations on the generated nutshell models. These simulations replicated the loading conditions shown in Fig. 2 and explained in **Section 5.2**. The compression of the nutshells was simulated as a nonlinear contact system between two rigid plates. An isotropic, linear-elastic model was employed to describe the global, geometry-dominated deformation of the nutshell at the macroscopic scale. As the material properties of the single layers, and specifically those for different loading directions, are not available, we assumed an isotropic linear-elastic response with a Young's Modulus of 2907 MPa (resulting from averaging the results of all our tensile and compression tests [7]) and a Poisson's ratio of 0.35, which is a typical value for wood [36]. A friction coefficient of 0.5 was set between the nutshell models and the plates (representative of the interaction between wood and steel [37]). The bottom plate was fixed ("encastre"), and the top plate was displaced by 5 mm with automated increment sizes ranging from 10^{-9} to 1, starting with 0.01. Mesh sensitivity was assessed by varying the element count until stresses and displacements changed by less than 2%, ensuring sufficient accuracy for the mechanical simulation. To identify regions prone to failure, we applied the maximum normal stress criterion, which is suitable for brittle materials [38]. Failure was predicted when the absolute maximum principal stress exceeded the corresponding tensile or compressive strength (**Table S2**). The sign of this stress component determined whether failure was classified as tensile or compressive.

6. Declaration of generative AI in scientific writing

During the preparation of this work, the author(s) used ChatGPT (OpenAI) in order to improve the clarity and conciseness of the language. After using this tool, the authors reviewed and edited the content as needed and take full responsibility for the content of the published article.

CRediT authorship contribution statement

Shajia Afrin Ali: Writing – review & editing, Writing – original draft, Visualization, Validation, Methodology, Investigation, Formal analysis, Data curation, Conceptualization. **Max David Mylo:** Writing – review & editing, Writing – original draft, Resources, Investigation, Funding acquisition, Data curation, Conceptualization. **Jonathan Perrin:** Writing – review & editing, Resources. **Timm Weitkamp:** Writing – review & editing, Resources. **Thomas Speck:** Writing – review & editing, Resources, Methodology, Funding acquisition, Conceptualization. **Claudia Fleck:** Writing – review & editing, Supervision, Project administration, Methodology, Conceptualization.

Funding

Thomas Speck and Max David Mylo gratefully acknowledge funding by the Deutsche Forschungsgemeinschaft (DFG, German Research Foundation) under Germany's Excellence Strategy – EXC-2193/1 – 390951807. Open Access funding enabled and organized by Projekt DEAL.

Declaration of competing interest

The authors declare that they have no known competing financial interests or personal relationships that could have appeared to influence the work reported in this paper.

Acknowledgements

The authors would like to express their sincere appreciation to N. Agarrado for providing pili nuts from Allen, Philippines. They also thank G. Razo (Manama Food Forest, Kidapawan City, Cotabato, Philippines) for sending freshly harvested fruits. The authors gratefully acknowledge S. Katabay and T. J. F. Isermeyer for conducting compression tests on whole and half nuts. Finally, the authors thank Dr. rer. nat. R. Meinke and R. Engelmayer (Chair of Materials Science & Engineering, Technische Universität Berlin, Germany) for their valuable assistance with imaging and mechanical testing on numerous occasions.

Appendix A. and Supplementary data

Appendix A and Supplementary data to this article can be found online at https://doi.org/10.1016/j.matdes.2026.115903.

Data availability

Data will be made available on request.

References

[1] M. Milwich, T. Speck, T. Stegmaier, H. Planck, Biomimetics and technical textiles: solving engineering problems with the help of nature's wisdom, Am. J. Bot. 93 (2006) 1455–1465, https://doi.org/10.3732/ajb.93.10.1455.
[2] P.T. Martone, M. Boller, I. Burgert, J. Dumais, J. Edwards, K. Mach, N. Rowe, M. Rüggeberg, R. Seidel, T. Speck, Mechanics without muscle: biomechanical inspiration from the plant world, Integr. Comp. Biol. 50 (2010) 888–907, https://doi.org/10.1093/icb/icq122.
[3] P. Schüler, T. Speck, A. Bührig-Polaczek, C. Fleck, Structure-function relationships in *Macadamia integrifolia* seed coats – fundamentals of the hierarchical microstructure, PLoS One 9 (2014) e102913, https://doi.org/10.1371/journal.pone.0102913.
[4] M. Sonego, C. Fleck, L.A. Pessan, Mesocarp of Brazil nut (Bertholletia excelsa) as inspiration for new impact resistant materials, Bioinspir. Biomim. 14 (2019) 056002, https://doi.org/10.1088/1748-3190/ab2298.
[5] R.K.B. Gallegos, D.C. Suministrado, R.M.C. Amongo, M.S. Madlangbayan, Some physical and mechanical properties of pili (Canarium ovatum Engl. cv. Katutubo) nut as a function of nut moisture content, Philipp. Agric. Sci. 96 (2013) 66.
[6] S. Schmier, M. Jentzsch, T. Speck, M. Thielen, Fracture mechanics of the endocarp of *Cocos nucifera*, Mater. Des. 195 (2020) 108944, https://doi.org/10.1016/j.matdes.2020.108944.
[7] S.A. Ali, M.D. Mylo, J. Perrin, T. Weitkamp, T. Speck, C. Fleck, Design across hierarchy: morphological and mechanical insights into pili nuts (Canarium ovatum), Mater. Des. 250 (2025) 115163, https://doi.org/10.1016/j.matdes.2025.115163.
[8] R.E. Coronel, Pili nut, Canarium ovatum Engl., Institute of Plant Genetics and Crop Plant Research/International Plant Genetic Resources Institute, Rome, Italy, 1996.
[9] L. Endonela, T. Borromeo, N. Altoveros, M.C. Bartolome, E.B. Timog, A. Alercia, F. López, A. Cerutti, R.J. Gentallan, in: Key Descriptors for Pili Nut (canarium Ovatum Engl.), United Nations and University of the Philippines, Rome, Italy, 2023, https://doi.org/10.4060/cc3704en.
[10] D.P. Updike, A. Kalnins, Axisymmetric behavior of an elastic spherical shell compressed between rigid plates, J. Appl. Mech. (1970), https://doi.org/10.1115/1.3408592.
[11] L. Pauchard, S. Rica, Contact and compression of elastic spherical shells: the physics of a 'ping-pong'ball, Philos. Mag. B 78 (1998) 225–233, https://doi.org/10.1080/13642819808202945.
[12] E. Stein, History of the Finite Element Method – Mathematics Meets Mechanics – Part I: Engineering Developments, Springer Berlin Heidelberg, Berlin, Heidelberg, Germany, 2014. doi:10.1007/978-3-642-39905-3_22.
[13] M.D. Mylo, S. Poppinga, Digital image correlation techniques for motion analysis and biomechanical characterization of plants, Front. Plant Sci. 14 (2024) 1335445, https://doi.org/10.3389/fpls.2023.1335445.
[14] R. Sachse, A. Westermeier, M. Mylo, J. Nadasdi, M. Bischoff, T. Speck, S. Poppinga, Snapping mechanics of the Venus flytrap (*Dionaea muscipula*), Proc. Natl. Acad. Sci. U. S. A. 117 (2020) 16035–16042, https://doi.org/10.1073/pnas.2002707117.
[15] S.A. Ali, M. Sonego, M. Salavati, C. Fleck, Influence of structure and geometry on the compressive deformation behavior of *Macadamia integrifolia* and Bertholletia excelsa shells: a validated finite element simulation study, Adv. Eng. Mater. 26 (2023) 2300723, https://doi.org/10.1002/adem.202300723.
[16] H.K. Celik, G. Kunt, A.E.W. Rennie, I. Akinci, Non-linear fem-based shattering simulation of shelled edible agricultural products: walnut shattering by nut cracker hand tool, Int. J. Technol. Eng. Stud. 3 (2017) 84–92, https://doi.org/10.20469/ijtes.3.40006-2.
[17] K. Onder, Cracking Simulation of Hazelnut Shell using Finite Element Method, Mitt. Klosterneuburg 70 (2020) 148–156. doi:https://www.weinobst.at/dam/jcr:7c641282-8182-4bb1-b62d-8ecc93a01f87/148-2020.pdf.
[18] H.K. Celik, N. Caglayan, A.E.W. Rennie, Nonlinear FEM based high-speed shell shattering simulation for shelled edible agricultural products: pecan fruit shattering, J. Food Process Eng 40 (2016), https://doi.org/10.1111/jfpe.12520.
[19] D. Coskun, D.T. Britto, W.Q. Huynh, H.J. Kronzucker, The role of silicon in higher plants under salinity and drought stress, Front. Plant Sci. 7 (2016) 210358, https://doi.org/10.3389/fpls.2016.01072.
[20] J.S. Jennings, M.H. Macmillan, A tough nut to crack, J. Mater. Sci. 21 (1986) 1517–1524, https://doi.org/10.1007/BF01114704.
[21] J.F.V. Vincent, Nuts,, MRS Online Proc, Libr 292 (1992) 35, https://doi.org/10.1557/PROC-292-35.
[22] M. Sonego, A. Morgenthal, C. Fleck, L.A. Pessan, Betholletia excelsa fruit: unveiling toughening mechanisms and biomimetic potential for advanced materials, Biomimetics 8 (2023) 509, https://doi.org/10.3390/biomimetics8070509.
[23] L. Striet, M.D. Mylo, O. Speck, P.W. Dondl, Modeling abscission of cacti branches, J. Mech. Phys. Solids 196 (2025) 105965, https://doi.org/10.1016/j.jmps.2024.105965.
[24] H.-C. Spatz, H. Beismann, F. Brüchert, A. Emanns, Th. Speck, Biomechanics of the giant reed *Arundo donax*, Philos. Trans. R. Soc. Lond. B Biol. Sci. 352 (1997) 1–10, https://doi.org/10.1098/rstb.1997.0001.
[25] M.D. Mylo, M. Hofmann, F. Balle, S. Beisel, T. Speck, O. Speck, Biomechanics of the parasite–host interaction of the European mistletoe, J. Exp. Bot. 73 (2022) 1204–1221, https://doi.org/10.1093/jxb/erab518.
[26] T. Steinbrecher, E. Danninger, D. Harder, T. Speck, O. Kraft, R. Schwaiger, Quantifying the attachment strength of climbing plants: a new approach, Acta Biomater. 6 (2010) 1497–1504, https://doi.org/10.1016/j.actbio.2009.10.003.
[27] C.S. Ross, Shapes in Math, Science and Nature: Squares, Kids Can Press Ltd, Triangles and Circles, 2014.
[28] C. Spura, Technische Mechanik 1. Stereostatik: Freischneiden und Gleichgewicht – mehr isses nicht!, Springer Fachmedien, Wiesbaden, 2024. doi:10.1007/978-3-658-46141-6.
[29] T. Mechanik, Teubner, Wiesbaden (2006), https://doi.org/10.1007/978-3-8351-9083-2.
[30] S.S. Shapiro, M.B. Wilk, An analysis of variance test for normality (complete samples), Syst. Zool. 52 (1965) 591–611, https://doi.org/10.1093/biomet/52.3-4.591.
[31] B.B. Schultz, Levene's test for relative variation, Syst. Zool. 34 (1985) 449–456, https://doi.org/10.2307/2413207.

[32] E. Ostertagova, O. Ostertag, J. Kováč, Methodology and application of the Kruskal-Wallis test, Appl. Mech. Mater. 611 (2014) 115–120, https://doi.org/10.4028/www.scientific.net/AMM.611.115.
[33] O.J. Dunn, Multiple comparisons using rank sums, Technometrics 6 (1964) 241–252, https://doi.org/10.2307/1266041.
[34] C.-H. Wang, Y.-W. Mai, Deformation and fracture of Macadamia nuts: Part 2: Microstructure and fracture mechanics analysis of nutshell, Int. J. Fract. 69 (1994) 67–85.
[35] R. Kikinis, S.D. Pieper, K.G. Vosburgh, 3D Slicer: A Platform for Subject-Specific Image Analysis, Visualization, and Clinical Support, in: F.A. Jolesz (Ed.), Intraoperative Imaging and Image-Guided Therapy, Springer New York, New York, NY, 2014: pp. 277–289. doi:10.1007/978-1-4614-7657-3_19.
[36] D.W. Green, J.E. Winandy, D.E. Kretschmann, Mechanical properties of wood. Wood handbook—Wood as an engineering material, FPL (1999), https://doi.org/10.2737/FPL-GTR-113.
[37] W.M. McKenzie, K. Melbourne, The frictional behaviour of Wood, Wood Sci. Technol. 2 (1968) 139–152, https://doi.org/10.1007/BF00394962.
[38] R.G. Budynas, J.K. Nisbett, Shigley's Mechanical Engineering Design, 10th ed., McGraw-Hill Education, New York, USA, 2015.
[39] J. Nader, J.C. Assaf, E. Debs, N. Louka, Innovative method for determining young's modulus of elasticity in products with irregular shapes: application on peanuts, Processes 11 (2023) 2532, https://doi.org/10.3390/pr11092532.